Full paper

Hybrid porous micro structured finger skin inspired self-powered electronic skin system for pressure sensing and sliding detection

Haotian Chen[a], Yu Song[b], Hang Guo[a], Liming Miao[b], Xuexian Chen[a], Zongming Su[b], Haixia Zhang[a,b,*]

[a] Academy for Advanced Interdisciplinary Studies, Peking University, Beijing 100871, China
[b] National Key Lab of Nano/Micro Fabrication Technology, Institute of Microelectronics, Peking University, Beijing 100871, China

A B S T R A C T

Fingertip is the most sensitive region in human body due to the unique fingerprint patterns and interlocked structure between epidermal-dermal, which amplify the tactile stimuli and enhance the sensitivity. Inspired by the complicated anatomical structure, we fabricated a finger skin inspired e-skin system composed of fingerprint inspired triboelectric generator (TENG), epidermal-dermal inspired hybrid porous microstructure (HPMS) pressure sensor and subcutaneous fat inspired fabric based porous supercapacitor (FPSC). The TENG is responsible for detecting sliding direction and speed with the help of the four spiral electrodes, which adopt the frequency rather than the amplitude to detect the signal to avoid interfere from the environment. The HPMS, on the one hand, integrates the advantages from both the microstructure and porous structure to enhance the sensitivity further. On the other hand, the sensitivity of HPMS sensor is tunable by designing the shape and porosity of the HPMS, which is proved by theory, simulation and experiment. The FPSC, which can tolerate some degree of compression, works to supply energy for the pressure sensor. In this way, the sensor system can work independently without external battery. As a proof-of-concept demonstration, this sensor system has been used to detect complex action including pressure and sliding. During this process, the pressure and sliding direction and speed can be detected simultaneously without connecting to external energy source, showing its potential application area in soft robot and wearable devices.

1. Introduction

Human skin is the largest organ covering the whole human body, which not only provides a protection against external stimuli but also takes charge of interacting with the outer environment [1]. Due to its fantastic features, electronic skin (e-skin) is proposed to mimic the properties of real human skin by transducing physical parameters such as pressure, sliding, temperature and other physiological variables into electronic signals, which open a new gate in many potential applications such as wearable devices [2,3], health monitoring [4,5], artificial prosthetics [6] and smart robots [7].

From the physiological view, human skin can be briefly divided into three layers—epidermis, dermis and subcutaneous layer [8]. Epidermis and dermis, in which there exists four kinds of mechanoreceptors, are mainly responsible for sensation of outer environment. According to the speed of adaptation behavior, mechanoreceptors can be classified into slowly adapting (SA) or fast adapting (FA). SA responds to sustained touch and pressure while FA responds to dynamic touch and vibration

stimuli [9,10]. Subcutaneous layer is the layer where the fat together with some blood vessels and nerves exists to supply energy for the skin system. It is worth mentioning that there is a unique structure—fingerprint, which only exists on the fingertip, with complex surface pattern to help enhance the sensitivity of human finger [9]. In this way, fingertip is the most sensitive organs providing us plenty of information.

Based on these physiological research results, scientists and engineers have adopted various methods to mimic these properties of the real skin. Resistance and capacitor sensor are two most common transducers mimicking SA as they can maintain the signals from the stimuli. Different from resistance and capacitor sensors, piezoelectric sensor [11,12] and triboelectric generator (TENG) [13,14] are two typical sensing mechanisms only responding to dynamic stimuli, which are very suitable for mimicking FA. Compared with piezoelectric sensor, TENG is more favorable due to its feather that all the materials have the triboelectric effect [15] while only some specific materials have the piezoelectric effect. Various inspiring research works

associated with TENG present its great potential in a lot of fields like energy harvester [16], self-powered sensor [17] and blue energy [18]. Self-powered sensor, which can generates signal by itself without battery, brings a lot of advantages in the application and saves much energy. It is regraded as the promising technology and hoped to be applied in many application fields like Internet of things (IoT) [19], implantable devices [20] and electronic skin [21].

In order to satisfy the requirement of both mechanical flexibility and electrical conductivity of e-skin, different materials including carbon nanotube [22,23], graphene [24–26], metal nanowire [27–29] and conductive polymer [30] are widely studied. What's more, plenty of microstructures (crack [3], wrinkle [31], micro-pyramid structure [32], micro-hairy [4] and porous structure [33]) are also designed and fabricated to enhance the performance of the devices. Besides the pressure sensor, more functional sensors including sliding sensor [34], bending sensor [22], temperature sensor [35] and chemical sensor [5] are also be deeply explored.

Apart from fabricating the single sensor, stretchable energy devices are also broadly investigated including flexible battery [36], solar cell [37] and supercapacitors [38], which is aim to supply energy for the stretchable sensor. Among them, supercapacitor (SC) is a promising energy storage devices due to its high power density, long cycling life and easy operation. Many materials like CNTs [39] and silver nanwires [40] with different structures [41] or functions like self-healing [42] are broadly explored. What's more, electronic system integrating SC with other devices like pressure sensor, photodetector [43], electrochromic device [44] and so on is the emerging research field attracting researchers from different backgrounds.

Currently, most research works focus on a single device, however, human skin is a complex system with plenty of function including both sensing element and power supply element, which should be included into the e-skin system. What's more, it is important to manufacture materials with tunable mechanical sensitivity, just like how human skin adopts different sensory cells for different kinds of forces. Last but not least, the structure of fingerprint should be exploited further as it is necessary for human to detect sliding due to its unique pattern, which can also be integrated into e-skin.

By mimicking diverse structures and functions of human skin system, we present a finger skin inspired multifunctional e-skin system integrating sliding sensing, pressure sensing and power supply element together. This e-skin system is composed of three layers functioned as sliding detection, pressure detection and energy supply, respectively. Different from traditional sliding sensors, which usually adopt a sensor array to detect sliding distance and direction, a fingerprint inspired TENG is demonstrated to realize the detection of both sliding direction and speed without external power. Furthermore, a hybrid porous microstructure (HPMS) is firstly proposed in this work, which not only increases the sensitivity of pressure sensor but also provides a way to obtain sensors with different sensitivities. At last, a fabric based porous supercapacitor (FPSC) is fabricated to power the HPMS piezoresistor, functioning like a subcutaneous fat to form an e-skin system. Fabric is an ideal material due to its flexibility and porosity [45]. As proof of concept, we demonstrate that our e-skin system can precisely perceive daily movement including both sliding and pressure simultaneously powered by its own energy element rather than external battery, which demonstrates it potential application in robotics and wearable devices.

2. Experimental section

2.1. Fabrication of the CNT-PDMS

CNTs was purchased from Boyu Co.,China with length of 10 μm. Firstly, 5 g CNTs were mixed with PDMS base (Dow Corning, Sylgard 184) at the mass fraction we needed. 20 ml toluene was added into the mixture of CNT and PDMS with volume ratio of 4:1 to make the CNT disperse uniformly in PDMS. Then the mixture of these three materials

was stirred for 6 h using magnetic stirring apparatus. After CNTs was well mixed into PDMS with the help of toluene, the mixture was poured into an evaporating dish to evaporate residual toluene. The cross-linking agent of PDMS can not be added until the toluene was thoroughly removed.

2.2. Fabrication of the fingerprint inspired TENG

The uncured CNT-PDMS and its cross-linking agent were shaped using a 3D-printed Aluminum alloy mold with the spiral structure. Then the CNT-PDMS together with the mold was baked at 70 °C for 2 h. After the spiral CNT-PDMS was solidified, pure liquid PDMS was poured onto the electrodes serving as a substrate and solidified with the CNT-PDMS together. In this way, the substrate was bonded with the electrodes and can be peel off together from the mold. The resistance of CNT-PDMS can be modulated by controlling the mass ratio of CNT and PDMS.

2.3. Fabrication of the CNT-PDMS with hybrid porous microstructure

Aluminum alloy molds with different microstructures like cone and pyramid were fabricated using 3D printer. The parameters including the diameter of the cone, the side length of the pyramid, the height and the side angle can be easily designed with the corresponding software. Uncured CNT-PDMS was firstly mixed with soluble micro particles and then the mixture was shaped into the mold mentioned above. In this work, the soluble particles are sugar particles, which were obtained with a commercial grinder. The size of the particles is in the range of 10–100 μm. With the similar method for fabricating spiral electrode, the CNT-PDMS with different shapes can be fabricated. At last, the sample containing sugar particles are immersed into water to remove the micro particles.

2.4. Fabrication of fabric based porous supercapacitor

The general CNT/cotton fabric electrodes are fabricated by using the drop-coating method. Firstly, the flexible cotton fabric (20 cm^2 is cleaned with ethanol and deionized water. Then, the CNT ink solution is prepared by dispersing 100 mg CNTs with 100 mg sodium dodecyl benzene sulfonate (SDBS) as a surfactant in 100 ml deionized water. After bath-sonicated for 4 h, the CNTs are dispersed uniformly. Then the cotton fabric is drop-coated using the CNT ink solution and dried at 90 °C. After 5 times of drop-dry process, the CNTs get saturated as the active materials. For the electrolyte, 6 g phosphoric acid (H3PO4) is mixed with 60 ml deionized water and 6 g polyvinyl alcohol (PVA) powder. The mixture is heated up to 85 °C under vigorous stirring until the solution becomes clear. Coated with the PVA/H3PO4 gel electrolyte, a cellulose separator is assembled with two pieces of CNT/cotton fabric electrodes. At last, the prepared solid state supercapacitor is left in the fume hood at room temperature to fully vaporize the excess water.

3. Results and discussion

3.1. Finger skin inspired multifunctional e-skin system

Fig. 1a schematically illustrates the anatomical structure of human finger skin consisting of epidermis, dermis and subcutaneous fat. On the epidermis, complex spiral-shaped fingerprint is the unique structure responsible for enhancing the sensitivity of sliding detection. Between epidermis and dermis, there exists a microstructure known to amplify and efficiently transfer the tactile stimuli. At the bottom, a subcutaneous fat layer is responsible for providing energy for human daily activities. Inspired from all the features mentioned above, a three-layer e-skin system, composed of a fingerprint inspired TENG responsible for sliding detection, a epidermal-dermal inspired HPMS piezoresistor, which is fabricated with carbon nanotube- polydimethylsiloxane (CNT-
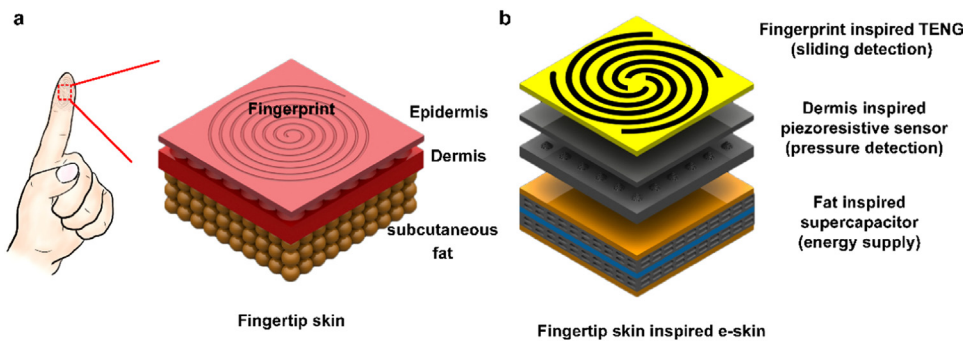
Fig. 1. Human finger skin inspired multi-functional e-skin system. a Structural and functional characteristics of human finger skin including fingerprint, epidermis, dermis and subcutaneous fat. b Schematic illustration of finger skin inspired e-skin system which consists of a TENG for sliding detection, a HPMS piezoresistor for pressure sensing and a super-capacitor for energy supply.
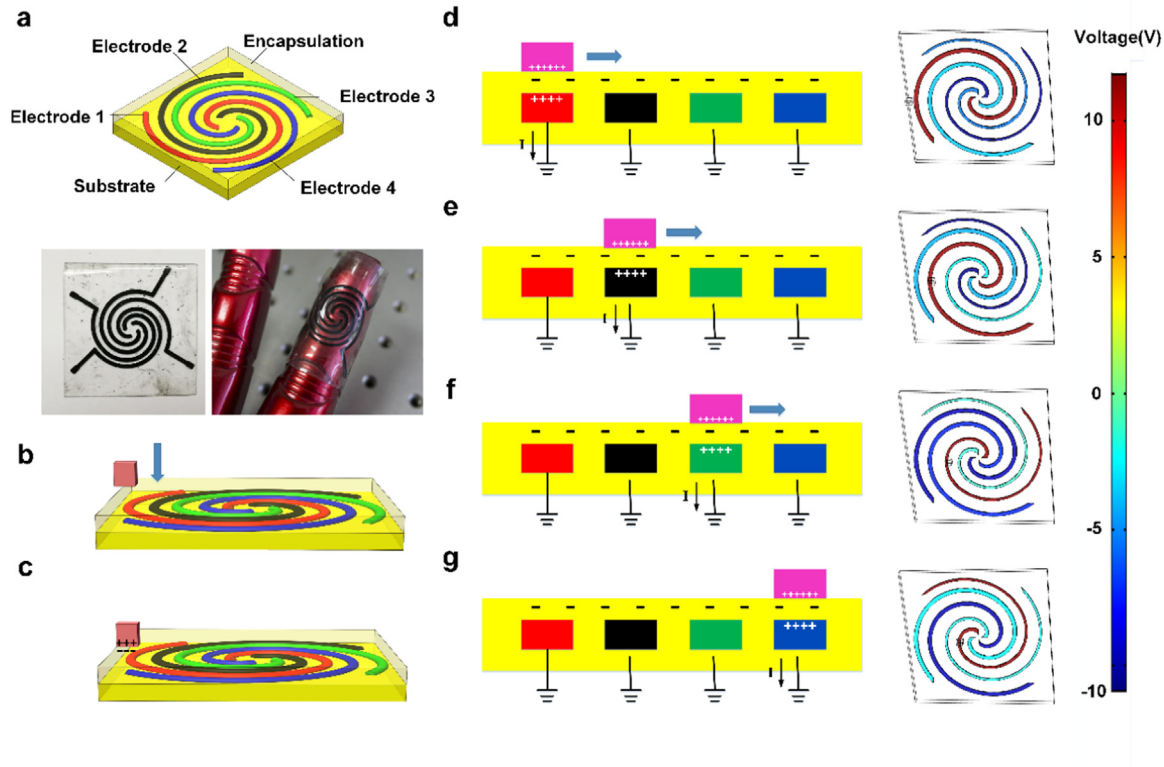

Fig. 2. Fingerprint inspired TENG and its working principle. a Schematic diagram and photo of the device containing four spiral electrodes. b-c Process of contact electrification. d-g Working principle of this device together with the simulation result indicating how the potential changes.

PDMS), responsible for pressure detection and a subcutaneous fat inspired FPSC responsible for energy supply, is demonstrated in Fig. 1b.

3.2. Fingerprint-inspired TENG for sliding detection

The fingerprint-inspired TENG consists of a PDMS substrate and four CNT-PDMS spiral electrodes, each of which works as a single-friction-surface TENG (STENG) [46], respectively (Fig. 2a). For convenience, four electrodes are marked in different colors, red (E_1), black (E_2), green (E_3) and blue (E_4), respectively. The coin-sized dimension of the sensor enable its broad integration in many fields. The small size and thin thickness of the sensor enable that the device can be easily attached on many non-planar surfaces. As a demonstration, the sensor is covered on a finger of a robot hand. As it is fabricated with soft materials, the sensor can be easily covered on the finger surfaces, which broaden its application areas.

The pattern of electrodes is carefully designed to ensure no matter which direction an external object sliding across the surface of the sensor, each STENG can be activated one by one. Due to the specialized

pattern of electrodes, the response sequence of the four STENGs is dependent on the sliding direction, which provide a way for direction detection.

Working principle of this sensor is demonstrated as follows. When an outer object contacts the sensor, a charge separation will be generated due to the contact electrification effect (Fig. 2b-c). Taking one direction as example, when the outer object moves close to E_1, much more positive charges will be induced on E_1 compared with the other three electrodes due to the electrostatic induction effect. In this way, a higher potential is produced on E_1 shown in Fig. 2d. As the outer object continues to move, E_2 will induce more positive charges while the number of positive charges on E_1 decreases dramatically. So the potential of E_2 gets to the highest among the four electrodes (Fig. 2e), thus generating a current flowing from the electrode to the ground. Then the outer object goes on to move, E_3 gets to the highest potential as shown in Fig. 2f. Similar potential distribution can be inferred when the object moves to E_4 as shown in Fig. 2g. Finite element method (FEM) is also carried out to verify the whole process.

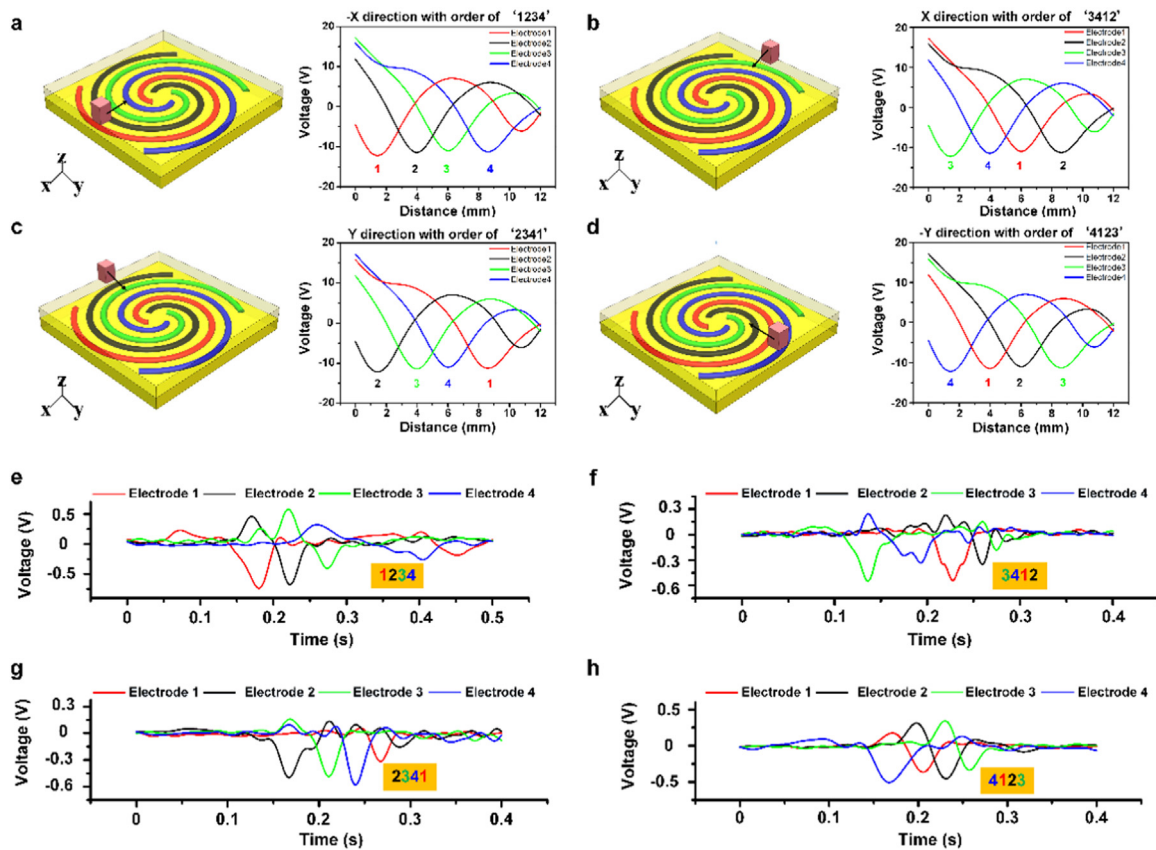As the outer object moves along -X direction as shown in Fig. 3a, all

Fig. 3. Simulation results and experiment tests showing how to detect sliding motion from different directions with this sensor and how to calculate movement speed. a-d Simulation demonstrating how the voltages changes when the external object moves along different directions. e-f Real voltage can give obvious responses when an outer object moves along different directions showing that TENG detect the sliding motion by frequency.

of the voltages from 4 electrodes goes down until it definitely located above the E_1, where the voltage of E_1 gets the lowest. As the object continues to move along this direction, the voltage of E1 begins to increase while the other three voltages from E_2-E_4 continue to decrease. Similarly, the voltage of E_2 reaches the lowest when the object moves above E_2. When the object moves to the center of the sensor, E_3 and E_4 get to the lowest voltages one after another. By detecting the order of the four electrodes getting the lowest voltage, which is '1234' in this condition, the sliding direction can be inferred.

In the similar way, when the object moves along +X, +Y and –Y directions, the corresponding voltage sequences are '3412', '2341' and '4123', respectively, as shown in Fig. 3b-d. By increasing the number of electrode in the sensor, the detectable directions can be increased from four to more directions.

Besides the direction detection, the sensor can also be responsible for displacement detection according to the number of voltage valleys (N) and structural parameters of width of the electrode (w) and gap between nearest two electrodes (g) by calculating $N * (w+g)$. What's more, the sliding speed can also be inferred from the displacement calculated above and the time intervals (t) between two valleys.

In order to demonstrate the practical performance of this fingerprint-shaped sliding sensor, human finger is adopted as the moving object to move across the sliding sensor and the test results from four directions are demonstrated in Fig. 3e-h.

Fig. 3e demonstrates the movement of human finger along the –X direction with sequence of '1234'. From the waveform, it can be inferred that at the beginning of the movement, the speed is as fast as $(w+g)/t = 2\,mm/0.4\,s = 5\,mm/s$ due to the short time interval between the valleys of E_1 and E_2. After the finger gets to E_3, the speed is dramatically decease to $(w+g)/t = 2\,mm/2.3\,s = 0.87\,mm/s$. In this way, this fingerprint-shaped STENG can not only tell the moving direction

but also reflect the moving details such as speed at some specific location interval.

The movement of human finger along the +Y direction is demonstrated in Fig. 3f. The speed in this direction is stable at 4 mm/s. Similar movements along +X and –Y directions are shown in Fig. 3g and h, respectively. No matter in what direction, both the displacement and speed can be calculated from analyzing the waveform. The output voltage and current can be found in Supporting Information Fig. S7.

One of the most significant feature of this TENG based sliding sensor is that it is dependent on the frequency rather than the amplitude of the output, which provides an efficient way of sliding detection no matter in what condition. Amplitude of TENG is usually affected by variable environmental factors such as humidity. By utilizing frequency, the output can reflect the characteristics of movement although the amplitude may be different. The peak-to-peak voltage in Fig. 3e is around 0.9 V while the value in Fig. 3f is only 0.6 V. This difference will not affect the result of displacement and speed, which dramatically enhances the reliability of the sensor.

3.3. Epidermal-dermal inspired HPMS

The HPMS is the combination of the microstructure and porous structure as shown in Fig. 4a, with corresponding SEM images shown in Fig. 4b and c, in which the pores are observed to be distributed uniformly. The microstructure is beneficial for enhancing the sensitivity by causing the non-uniform stress distribution during the pressure while the porous structure, which increase the contact area during the pressure, are usually utilized to enhance the sensitivity of the piezo-resistance sensor. Both of the structures are explored broadly. This hybrid structure in this work, which integrates the advantages from these two classic structures, can further increase the sensitivity. Finite
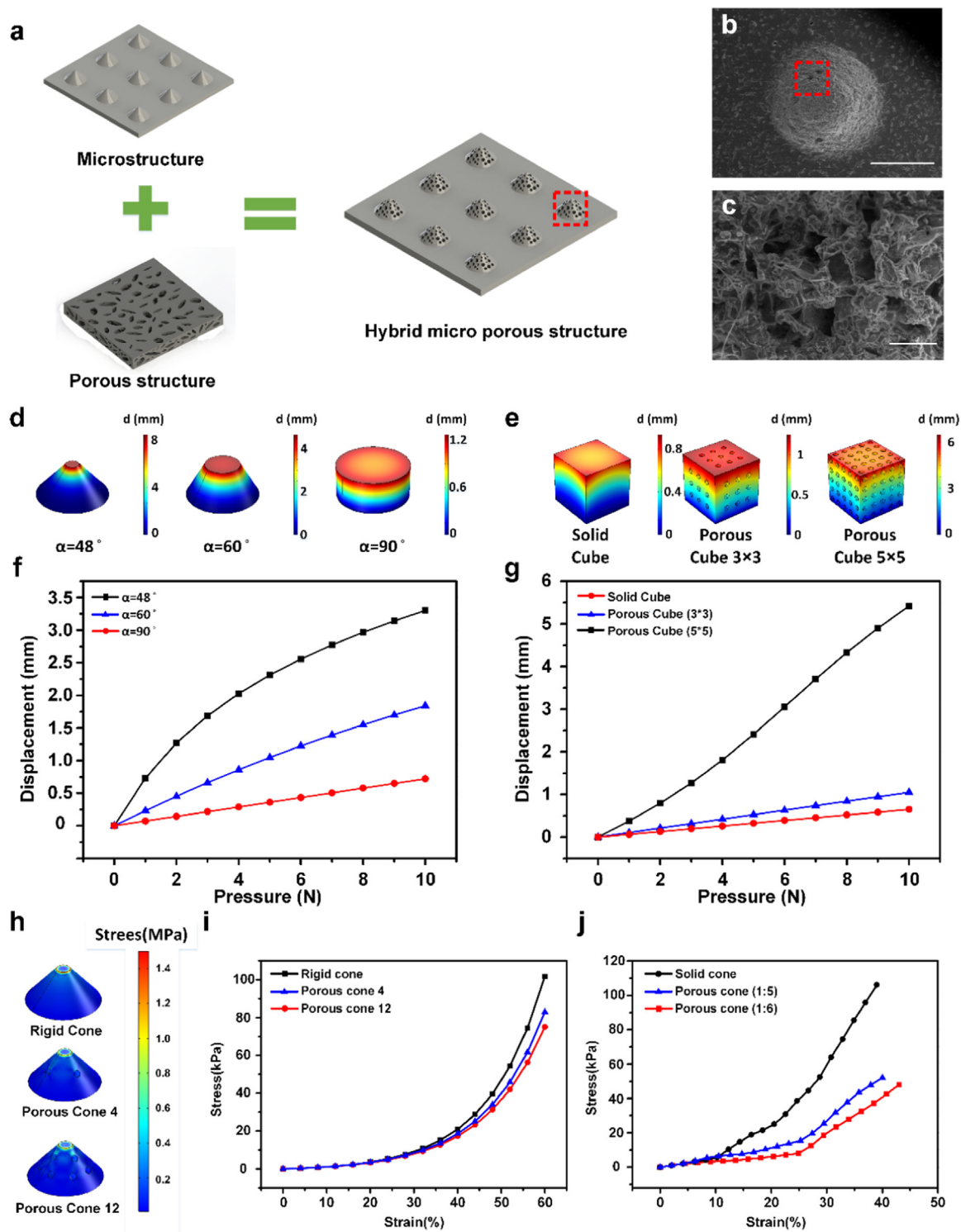
Fig. 4. Mechanical characterizes of HPMS. a Illustration of HPMS. b SEM image of a single HPMS. Scale bar: 1 mm. c enlarged SEM image of the single HPMS demonstrating its porous structure. Scale bar 100 μm d, f Simulation results showing stress-strain of microstructures with different sidewall angles. e, g Simulation results showing stress-strain of materials with different porosities. h-i Simulation results showing stress-strain of HPMS. j Experiment data to prove the result from simulation.

element Method (FEM) are adopted to study the mechanical char-acterizes.

The shape of microstructure is firstly studied. Fig. 4d and f shows the compressibility of solid materials with different 3D shapes. In the simulation, cone shape is taken as the basic shape. The size of bottom and the height are kept as the constant, while the sidewall angle, α, with respect to the base is varied. In this simulation, structures with sidewall angles of 48°, 60° and 90°, respectively, are selected to com-pare. From Fig. 4f, the smaller α is, meaning the sharper shape, the compressibility slope is larger, which implies that under the same pressure, cone with sharp angle has larger deformation.

When it comes to porosity, solid cube, porous cube 3 × 3 (each face

with the pattern of 3×3) and porous cube 5×5 (each face with the pattern of 5×5) are designed to study. From Fig. 4e and g, higher porosity will cause the more deformation under the same pressure. More pores, meaning more air space existing in the whole material, decrease the effective Young's modulus. In other words, higher porosity makes the material more 'softer'.

For the HPMS, corresponding simulation results is demonstrated in Fig. 4h and i, in which the porous structures are also simplified in the simulation model. Porous Cone 4 is the cone with four pores in it and Porous Cone 12 is the cone with twelve pores in it. All the pores have the same size. The effective Young's modulus is adopted to describe the relationship between the stress and strain by taking the shape and porosity into account. From the simulation, Porous Cone 12 has the smallest slope, meaning the smallest effective Young's modulus, which also follow the same trend in porous cube. In order to verify this simulation result, a micro solid cone sample, marded as Solid Cone, and two kinds of porosity of HPMS are fabricate by mixing with soluble micro particles at the mass ratio of 1:5 and 1:6, marked as Porous Cone (1:5) and Porous Cone (1:6), respectively. The test result in Fig. 4j shows that the solid cone sample has the largest effective Young's modulus while the sample with highest porosity has the lowest effective Young's modulus. In addition to the micro cone, pyramid with different porosity are also studied. The SEM images, simulation results and measurement results are shown in Supporting Information Fig. S1 and Figure S2. Compared with the micro cone, the effective Young's modulus is higher. In order to better display the HPMS, horizontal SEM images of these two kinds of HPMSs are demonstrated in Fig. S5.

After studying the mechanical characterizes of HPMS, piezoresistance can be better explored. The piezoresistance is measured by detecting the contact resistance between a flat CNT-PDMS and HPMS CNT-PDMS as shown in Fig. 5a. As cone is very easy to be compressed into a frustum of cone, a model of frustum of cone is established to study how the shape and porosity can affect the performance of the pressure sensor. Under the perfect elasticity assumption, key parameters including the radius of bottom circle, r, the sidewall angle, α, the radius of top circle before compression, r_1, the height before compression, l, the radius of top circle after compression, r_2, the height after compression, l' and the radius of the micro pore, r_s, are defined shown in Fig. 5b. The test instrument is shown in Fig. 5c. Among all the parameters, r, α, l and r_s can be defined by fabricating different 3D printing molds and mixing different sizes of soluble micro particles. In order to better analyze how the shape and porosity can influence the performance of the device, the radius of bottom circle, r, and the height, l, are taken as the constant. In this way, other key parameters can be written as follows:

$$r_1 = r - 2 \cdot l \cdot \cot \alpha \tag{1}$$

$$r_2 = r - 2 \cdot (l - \Delta l) \cdot \cot \alpha \tag{2}$$

Where $\Delta l = l - l'$ is the changed height after compression. From the formula, r_1 is only associated with the side angle and the r_2 is associated with the side angle and the changed height.

The sensitivity of the device is defined as

$$S_e = \frac{\Delta R / R}{P} \tag{3}$$

Where ΔR is the change in resistance cause by stress P and R is the original resistance. According to the definition of resistance:

$$R = \frac{l}{\delta S} \tag{4}$$

Where l is the length, S is the cross area and δ is conductivity. Here, the conductivity can be modulated by the mixing different ratios of CNTs and PDMS, which is kept as constant. so the sensitivity can be described as

$$S_e = \left| \frac{\Delta l / l}{P} \right| + \left| \frac{\Delta S / S}{P} \right| \tag{5}$$

Where ΔS is the changed contact area after compression.

For a HPMS, ΔS is composed of two parts. One is the enlarged top surface area, ΔS_1 caused by compression due to the shape and the other is the enlarged inner contact area, ΔS_2, due to the porosity. In our model, S, ΔS_1 and ΔS_2 can be expressed as:

$$S = \pi r_1^2 \tag{6}$$

$$\Delta S_1 = \pi (r_2^2 - r_1^2) \tag{7}$$

$$\Delta S_2 = \frac{\Delta V (1 - \eta)}{V_p} \cdot S_p = \frac{\frac{1}{3} \Delta l (r_1^2 + r_2^2 + r_1 r_2) \cdot \pi \cdot (1 - \eta)}{\frac{4}{3} \cdot \pi \cdot r_s^3} \cdot \pi \cdot r_s^2 \tag{8}$$

Where V_p is the volume of a single air pore, which is considered as a ball and η is the relative density defined as $\eta = \frac{\rho^*}{\rho_s}$. That is, the density of HPMS CNT-PDMS, ρ^*, divided by that of the solid form of CNT-PDMS, ρ_s. The smaller the relative density is, the larger porosity the material has. S_p is the contact area when the air pore are completely compressed. So $\frac{\Delta V (1 - \eta)}{V_p}$ is the number of compressed air pores and $\frac{\Delta V (1 - \eta)}{V_p} \cdot S_p$ is the total changed areas caused by compressed porous structure.

After omitting higher order terms, sensitivity of the pressure sensor is expressed as

$$S_e \sim \left(\frac{\pi \cdot (1 - \eta) \cdot l}{4 r_s} + \frac{2 \cdot \cot \alpha}{r/l - 2 \cdot \cot \alpha} + 1 \right) \frac{1}{E} \tag{9}$$

In this formula, $\frac{1}{E} = \frac{\Delta l / l}{P}$ is reciprocal of Young's modulus, E. Detailed calculation process is discussed in Supporting Information. From the formula, the sensitivity is inverse proportional to the effective Young's modulus, E, the sidewall angle, α, the size of micro space, r_s and the relative density, η. In this way, the sensitivity can be well tunable by using all these parameters. Detailed calculation is demonstrated in Supporting Information Fig. S3

Fig. 5d shows the performances of different samples, including Solid Cone, Porous Cone (5:1) and Porous Cone (6:1). The sensitivity of these three samples are 15.5 kPa^{-1}, 22.4 kPa^{-1} and 35.7 kPa^{-1}, respectively. The measurement results is in conformity with the theory that Porous Cone (6:1) with the largest porosity has the highest sensitivity. The two sensitivity regions are caused by the porous structure, the effective Young's modulus of which also has two regions shown in Fig. 4j. According to the formula of sensitivity, the performance of the device is closely associated with the effective Young's modulus, thus producing the two sensitivity regions.

What's more, the temporal resistance changes for different stimuli of the strain sensor under cyclical pressure (Pressure: 0.1 N and 1 N) demonstrates its durability for sensing different pressures (Fig. 5e). In addition, the response time of this sensor is very fast. In the contact process, the response time is 107 ms while in the separate process, the response time is 80 ms as show in Fig. 5f.

3.4. Subcutaneous fat inspired FPSC

The structure of the FPSC is schematically illustrated in Fig. 5g. The electrode is a piece of CNT fabric, which is fabricated by simply dip-coating method. PVA/H$_3$PO$_4$ is chosen as the solid electrolyte enabling its stability under compression. A cellulose separator is assembled with two pieces of functional layer consisting of CNT-fabric electrode and PVA/H$_3$PO$_4$. The fabrication process has been explored by our group before [47].

In order to evaluate the electrochemical performance of the FPSC, the device is tested through cyclic voltammetry (CV), galvanostatic charge-discharge (GCD), Nyquist plots, Ragone plots, and cycling stability using an electrochemical workstation. Fig. 5h demonstrates the CV curves of the device with the scan rates ranging from 10 mV/s to
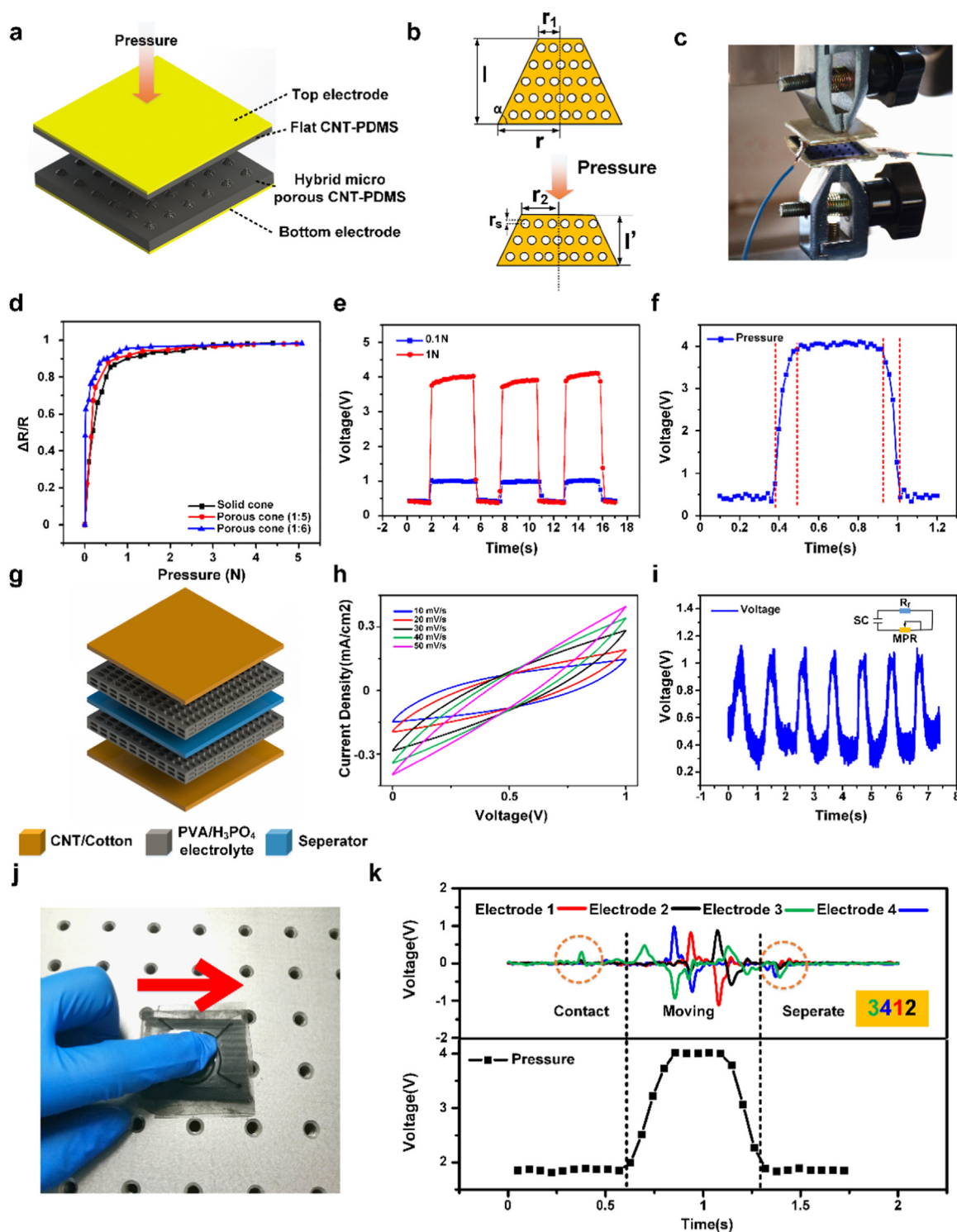
Fig. 5. Piezoresistance of HPMS and its combination with the FPSC and TENG working as a system. a Schematic diagram of the pressure sensor. b Key geometric parameters to describe the deformation of the microstructure. c Experiment equipment for piezoresistance test. d piezoresistance result demonstrating the relationship of changed resistance and pressure. e The resistance changes under a repeated pressure. f Response time of the device. g Schematic illustration of the structure of FPSC. h CV curves of FPSC. i The output of the pressure sensor powered by the FPSC. j A demonstration shows that the sensor system can detect complex action powered by its own energy device. k the outputs from TENG and pressure sensor can reflect the complex action from j.

200 mV/s at a stable potential window. The CV curves retain their quasi- rectangular shape and are approximately symmetrical about the zero-current line, indicating the ideal double-layer electrochemical behavior. Other electrochemical characterizes are shown in Support Information S4.

The FPSC was charged by a commercial current source(MAISHENG

DC power supply MS-155D) at first. Then the pressure sensor is series connected with a reference resistance and both of them are powered by the FPSC as shown in the inset of Fig. 5i. Under cyclic pressure, our pressure can give stable response with the FPSC working as a power supply, shown in Fig. 5i. As the pressure sensor can be powered by the supercapacitor and TENG is a self-powered device, the whole sensor

system can work without external battery.

3.5. Simultaneous multiple stimuli sensing

This sensor system can detect pressure and sliding simultaneously. Fig. 5j shows an operation of a combination action including both pressure and sliding and Fig. 5k demonstrates the responses from the TENG and pressure sensor. Detailed circuit diagram can be found in Supporting Information Fig. S5. When the finger contact the sensor system, TENG gives a response. Then the finger begins to slide and pressure on this device, both the TENG and pressure sensor start to work and reflect its dynamic pressure and sliding direction and speed at the same. At last, the finger separates from the sensor system. There is a slight pressure response, but the TENG give a clear signal. During this whole process, there is no external power connected to the device, the supercapacitor is responsible for supplying energy for the device.

4. Conclusion

By mimicking the structure and function of real skin, we present a finger skin inspired e-skin system which can sense pressure and sliding simultaneously without outer power source. The fingerprint inspired TENG provides a self-powered method to detect sliding direction and sliding speed in a digitalized way by analyzing the response order and frequency of four spiral STENGs. What's more, a new HPMS conductive elastomer is fabricated to detect pressure. The HPMS is a combination of microstructure and porous structure and integrates the advantages from both of them, thus further enhancing the sensitivity of the pressure sensor. By designing different shapes of microstructures and porosities, the sensitivity can be well modulated to adapt in different application areas. In addition, a FPSC, which mimics the function of subcutaneous fat, is fabricated to act as the power source of this sensor system. The CNT-fabric based electrode and solid electrolyte enable the supercapacitor to work stably under some degree of compression. As a demonstration, this system is used to detect complex action including pressure and sliding. In this process, the pressure and sliding direction and speed can measured simultaneously without connecting to external energy source, showing its great potential in areas like wearable devices and soft robot.

Acknowledgement

Appendix A. Supplementary material

Supplementary data associated with this article can be found in the online version at doi:10.1016/j.nanoen.2018.07.001.

References

[1] M.L. Hammock, A. Chortos, B.C.K. Tee, J.B.H. Tok, Z. Bao, Adv. Mater. 25 (2013) 5997–6038.
[2] Q. Hua, J. Sun, H. Liu, R. Bao, R. Yu, J. Zhai, C. Pan, Z.L. Wang, Nat. Commun. 9 (2018) 244.
[3] D. Kang, P.V. Pikhitsa, Y.W. Choi, C. Lee, S.S. Shin, L. Piao, B. Park, K.-Y. Suh, T.-i. Kim, M. Choi, Nature 516 (2014) 222–226.
[4] C. Pang, J.H. Koo, A. Nguyen, J.M. Caves, M.G. Kim, A. Chortos, K. Kim, P.J. Wang, J.B.H. Tok, Z. Bao, Adv. Mater. 27 (2015) 634–640.
[5] W. Gao, S. Emaminejad, H.Y.Y. Nyein, S. Challa, K. Chen, A. Peck, H.M. Fahad, H. Ota, H. Shiraki, D. Kiriya, Nature 529 (2016) 509.
[6] J. Kim, M. Lee, H.J. Shim, R. Ghaffari, H.R. Cho, D. Son, Y.H. Jung, M. Soh, C. Choi, S. Jung, Nat. Commun. 5 (2014) 5747.
[7] D. Rus, M.T. Tolley, Nature 521 (2015) 467.
[8] J. Dargahi, S. Najarian, Int. J. Med. Robot. Comput. Assist. Surg. 1 (2004) 23–35.
[9] V.E. Abraira, D.D. Ginty, Neuron 79 (2013) 618–639.
[10] R.S. Johansson, J.R. Flanagan, Nat. Rev. Neurosci. 10 (2009) 345–359.
[11] M. Ha, S. Lim, J. Park, D.S. Um, Y. Lee, H. Ko, Adv. Funct. Mater. 25 (2015) 2841–2849.
[12] I. Lee, H.J. Sung, Exp. Fluids 26 (1999) 27–35.
[13] S.H. Wang, L. Lin, Z.L. Wang, Nano Energy 11 (2015) 436–462.
[14] L. Lin, Y. Xie, S. Wang, W. Wu, S. Niu, X. Wen, Z.L. Wang, ACS Nano 7 (2013) 8266–8274.
[15] Z.L. Wang, Acs Nano 7 (2013) 9533–9557.
[16] X.L. Cheng, B. Meng, X.X. Chen, M.D. Han, H.T. Chen, Z.M. Su, M.Y. Shi, H.X. Zhang, Small 12 (2016) 229–236.
[17] H.X. Wu, Z.M. Su, M.Y. Shi, L.M. Miao, Y. Song, H.T. Chen, M.D. Han, H.X. Zhang, Adv. Funct. Mater. (2018) 28.
[18] J. Chen, J. Yang, Z.L. Li, X. Fan, Y.L. Zi, Q.S. Jing, H.Y. Guo, Z. Wen, K.C. Pradel, S.M. Niu, Z.L. Wang, Acs Nano 9 (2015) 3324–3331.
[19] Z.L. Wang, Mater. Today 20 (2017) 74–82.
[20] Y. Ma, Q. Zheng, Y. Liu, B.J. Shi, X. Xue, W.P. Ji, Z. Liu, Y.M. Jin, Y. Zou, Z. An, W. Zhang, X.X. Wang, W. Jiang, Z.Y. Xu, Z.L. Wang, Z. Li, H. Zhang, Nano Lett. 16 (2016) 6042–6051.
[21] Y. Yang, H.L. Zhang, Z.H. Lin, Y.S. Zhou, Q.S. Jing, Y.J. Su, J. Yang, J. Chen, C.G. Hu, Z.L. Wang, Acs Nano 7 (2013) 9213–9222.
[22] H. Chen, Z. Su, Y. Song, X. Cheng, X. Chen, B. Meng, Z. Song, D. Chen, H. Zhang, Adv. Funct. Mater. (2017) 27.
[23] D.J. Lipomi, M. Vosgueritchian, B.C. Tee, S.L. Hellstrom, J.A. Lee, C.H. Fox, Z. Bao, Nat. Nanotechnol. 6 (2011) 788–792.
[24] J. Park, M. Kim, Y. Lee, H.S. Lee, H. Ko, Sci. Adv. 1 (2015) e1500661.
[25] S.-H. Bae, Y. Lee, B.K. Sharma, H.-J. Lee, J.-H. Kim, J.-H. Ahn, Carbon 51 (2013) 236–242.
[26] S. Chun, A. Hong, Y. Choi, C. Ha, W. Park, Nanoscale 8 (2016) 9185–9192.
[27] Y.C. Lai, B.W. Ye, C.F. Lu, C.T. Chen, M.H. Jao, W.F. Su, W.Y. Hung, T.Y. Lin, Y.F. Chen, Adv. Funct. Mater. 26 (2016) 1286–1295.
[28] M. Shi, J. Zhang, H. Chen, M. Han, S.A. Shankaregowda, Z. Su, B. Meng, X. Cheng, H. Zhang, ACS nano 10 (2016) 4083–4091.
[29] M. Amjadi, A. Pichitpajongkit, S. Lee, S. Ryu, I. Park, ACS Nano 8 (2014) 5154–5163.
[30] Y. Wang, C. Zhu, R. Pfattner, H. Yan, L. Jin, S. Chen, F. Molina-Lopez, F. Lissel, J. Liu, N.I. Rabiah, Sci. Adv. 3 (2017) e1602076.
[31] L. Miao, X. Cheng, H. Chen, Y. Song, H. Guo, J. Zhang, X. Chen, H. Zhang, J. Micromech. Microeng. 28 (2017) 015007.
[32] H.-H. Chou, A. Nguyen, A. Chortos, J.W. To, C. Lu, J. Mei, T. Kurosawa, W.-G. Bae, J.B.-H. Tok, Z. Bao, Nat. Commun. 6 (2015) 8011.
[33] H. Chen, L. Miao, Z. Su, Y. Song, M. Han, X. Chen, X. Cheng, D. Chen, H. Zhang, Nano Energy 40 (2017) 65–72.
[34] Z. Su, H. Wu, H. Chen, H. Guo, X. Cheng, Y. Song, X. Chen, H. Zhang, Nano Energy 42 (2017) 129–137.
[35] N.T. Tien, S. Jeon, D.I. Kim, T.Q. Trung, M. Jang, B.U. Hwang, K.E. Byun, J. Bae, E. Lee, J.B.H. Tok, Adv. Mater. 26 (2014) 796–804.
[36] R. Kumar, J. Shin, L. Yin, J.M. You, Y.S. Meng, J. Wang, Adv. Energy Mater. (2017) 7.
[37] K. Chu, B.G. Song, H.I. Yang, D.M. Kim, C.S. Lee, M. Park, C.M. Chung, Adv. Funct. Mater. 28 (2018).
[38] Y. Song, H. Chen, Z. Su, X. Chen, L. Miao, J. Zhang, X. Cheng, H. Zhang, Small (2017) 13.
[39] Y. Song, X.X. Chen, J.X. Zhang, X.L. Cheng, H.X. Zhang, J. Micro. Syst. 26 (2017) 1055–1062.
[40] L.X. Shen, L.H. Du, S.Z. Tan, Z.G. Zang, C.X. Zhao, W.J. Mai, Chem. Commun. 52 (2016) 6296–6299.
[41] W.J. Liu, N.S. Liu, Y.L. Shi, Y. Chen, C.X. Yang, J.Y. Tao, S.L. Wang, Y.M. Wang, J. Su, L.Y. Li, Y.H. Gao, J. Mater. Chem. A 3 (2015) 13461–13467.
[42] Y. Yue, N. Liu, Y.A. Ma, S.L. Wang, W.J. Liu, C. Luo, H. Zhang, F. Cheng, J.Y. Rao, X.K. Hu, J. Su, Y.H. Gao, Acs Nano 12 (2018) 4224–4232.
[43] Y. Yue, Z.C. Yang, N.S. Liu, W.J. Liu, H. Zhang, Y.A. Ma, C.X. Yang, J. Su, L.Y. Li, F. Long, Z.G. Zou, Y.H. Gao, Acs Nano 10 (2016) 11249–11257.
[44] Y. Song, X.L. Cheng, H.T. Chen, J.H. Huang, X.X. Chen, M.D. Han, Z.M. Su, B. Meng, Z.J. Song, H.X. Zhang, J. Mater. Chem. A 4 (2016) 14306.
[45] K. Cherenack, L. Van Pieterson, J. Appl. Phys. 112 (2012).
[46] B. Meng, W. Tang, Z. Too, X. Zhang, M. Han, W. Liu, H. Zhang, Energy Environ. Sci. 6 (2013) 3235–3240.
[47] Y. Song, J. Zhang, H. Guo, X. Chen, Z. Su, H. Chen, X. Cheng, H. Zhang, Appl. Phys. Lett. 111 (2017) 073901.